Pore-scale analysis of the minimum liquid film thickness around elongated bubbles in confined gas-liquid flows

M. Magnini*, A. M. Beisel, A. Ferrari, J. R. Thome

Laboratory of Heat and Mass Transfer (LTCM), Ecole Polytechnique Fédérale de Lausanne (EPFL), EPFL-STI-IGM-LTCM, Station 9, CH-1015 Lausanne, Switzerland

Abstract

The fluid mechanics of elongated bubbles in confined gas-liquid flows in micro-geometries is important in pore-scale flow processes for enhanced oil recovery and mobilization of colloids in unsaturated soil. The efficiency of such processes is traditionally related to the thickness of the liquid film trapped between the elongated bubble and the pore's wall, which is assumed constant. However, the surface of long bubbles presents undulations in the vicinity of the rear meniscus, which may significantly decrease the local thickness of the liquid film, thus impacting the process of interest. This study presents a systematic analysis of these undulations and the minimum film thickness induced in the range $\mathrm{Ca} = 0.001 - 0.5$ and $\mathrm{Re} = 0.1 - 2000$. Pore-scale Computational Fluid Dynamics (CFD) simulations are performed with a self-improved version of the opensource solver ESI OpenFOAM which is based on a Volume of Fluid method to track the gas-liquid interface. A lubrication model based on the extension of the classical axisymmetric Bretherton theory is utilized to better understand the CFD results. The profiles of the rear

*Corresponding author. Tel.: +41 021 6937343.
Email address: mirco.magnini@epfl.ch (M. Magnini)

meniscus of the bubble obtained with the lubrication model agree fairly well with those extracted from the CFD simulations. This study shows that the Weber number of the flow, $We = Ca\,Re$, is the parameter that best describes the dynamics of the interfacial waves. When $We < 0.1$, a single wave crest is observed and the minimum film thickness tends to an asymptotic value, which depends on the capillary number, as $We \to 0$. Undulations dampen as the capillary number increases and disappear completely when $Ca = 0.5$. When $We > 0.1$, a larger number of wave crests becomes evident on the surface of the rear meniscus of the bubble. The liquid film thickness at the crests of the undulations thins considerably as the Reynolds number is increased, down to less than 60% of the value measured in the flat film region. This may significantly influence important environmental processes, such as the detachment and mobilization of micron-sized pollutants and pathogenic micro-organisms adhering at the pore's wall in unsaturated soil.
Keywords: Bubbles, Capillary Flow, Lubrication Model, Volume of Fluid, Interfacial Waves

1. Introduction

Understanding the dynamics of confined gas-liquid flows in micro-geometries is key to a wide variety of problems, ranging from industrial processes to environmental applications such as enhanced oil recovery [1], carbon dioxide sequestration [2], and mobilization of colloids in unsaturated soil [3, 4].

In water-saturated soil, gas bubbles may be generated by various processes [5]: entrapment of air as the water table fluctuates, organic and biogenic activities, emergence of gas from solution as the aqueous phase pres-

sure drops, hydraulic fracturing, etc. Gas-liquid interfaces are effective in detaching micron-sized colloids adhering on the pore walls due to the action of capillary forces [5, 3, 6, 7]. Detachment and transport of pollutants and pathogenic micro-organisms in unsaturated soil is of paramount environmental interest, as it influences the quality of drinking water resources [8, 9, 4, 10]. Pore-scale experiments are typically performed by injecting a bubble within a microfluidic channel of rectangular or trapezoidal cross-section [11, 10, 12], where colloidal particles are initially deposited. These experiments emphasized that the main factors influencing the particle detachment efficiency are the liquid-air interface velocity and interfacial tension [3, 4, 12]. When a gas bubble is displaced by liquid within a micro-geometry, this traps a thin liquid film against the pore's wall [13]. Recently, it has been postulated that the topology and thickness of the liquid film have a dramatic impact on the colloid detachment rate [14], with the detachment efficiency being maximum when the liquid film thickness is on the order of the colloid size.

It is well known from traditional fluid mechanics that the thickness h_0 of the liquid film around elongated bubbles is determined by the interplay between capillary and viscous forces, which is quantified by the capillary number [13, 15], $\mathrm{Ca} = \mu U/\sigma$, where μ indicates the liquid dynamic viscosity, σ the surface tension and U the velocity of the bubble, and by the interplay between inertial and viscous forces, which is quantified by the Reynolds number [16, 17, 18], $\mathrm{Re} = \rho UL/\mu$, where L is a characteristic length of the channel cross-section and ρ is the liquid density. Simple empirical correlations have been proposed to estimate h_0 as a function of Ca and Re, see e.g. Aussillous and Quéré [16], Han and Shikazono [19] and Langewisch

and Buongiorno [20], and these have been utilized to interpret experimental observations about colloid detachment performances [3, 14, 12].

However, the liquid film thickness around elongated bubbles is not constant, as undulations may appear near the bubble tail and make the liquid film significantly thinner than h_0 [21, 22, 23, 24], which is the thickness measured at a location which is sufficiently distant from the front and rear menisci of the bubble, where the liquid film is flat. To the authors' knowledge, only two studies reported values of the minimum film thickness induced by these undulations: Bretherton [13] performed a lubrication analysis valid at $\mathrm{Ca} \ll 1$ and $\mathrm{Re} \ll 1$, which suggested that the minimum thickness h_{min} is a constant fraction of the uniform film thickness, $h_{min} = 0.716 h_0$; Giavedoni and Saita [22] performed numerical simulations in the range $\mathrm{Re} = 0 - 50$ and observed that the minimum film thickness decreased with increasing Re, while the undulations amplitude for $\mathrm{Re} \ll 1$ was considerably smaller than the value predicted by the Bretherton's model when $\mathrm{Ca} > 10^{-3}$.

In the colloids detachment by a translating gas-liquid interface in a micropore, the thinner film at the bubble tail may promote the removal of wall-adhering particles. This may be the reason for the enhanced removal of wall-adhering bacteria by the rear meniscus of a long bubble translating in a rectangular microchannel in the study of Khodaparast et al. [12]. In microchannel flow boiling, Magnini and Thome [24] detected peaks of the heat transfer performance upon the crests of the bubble surface undulations, while it has been experimentally observed by Borhani et al. [25] that liquid film dryout initiates from the minimum film thickness regions in the proximity of the bubble tail. Therefore, a better understanding of the dynamics of the

capillary waves around elongated bubbles in confined gas-liquid flows is useful to enhance groundwater models and, more generally, would contribute to a better interpretation of experimental observations in many diverse problems that span different disciplines in science and engineering.

The objective of the present work is to perform a systematic analysis of the minimum liquid film thickness induced by the undulations appearing on the surface of long bubbles in confined gas-liquid flows, in the range $\mathrm{Ca} = 0.001 - 0.5$ and $\mathrm{Re} = 0.1 - 2000$. CFD simulations of the elongated bubble flow at the pore scale based on a Volume Of Fluid (VOF) interface capturing method [26], and a lubrication model based on the work of de Ryck [17] to describe the liquid film dynamics, are utilized to generate numerical and theoretical bubble profiles. The minimum liquid film thickness values extracted from both the CFD simulations and the lubrication model results are compared, and their trends versus the governing nondimensional groups are investigated.

This article is organized as follows: in Section 2, a description of the problem is presented; the CFD model is introduced in Section 3; the lubrication model is described in Section 4; the CFD and lubrication models are benchmarked versus in-house experimental results in Section 5; the results of the analysis of the undulations are discussed in Section 6; finally, the practical implications of thinning film processes on colloid mobilization from solid substrates are debated in Section 7.

2. Description of the problem

An elongated gas bubble translates at a velocity U in a micro-pore filled with liquid. The pore is modelled as a channel of circular cross-section, with radius R. Figure 1 shows a sketch of the flow configuration under analysis. The flow field and the bubble profile are assumed axisymmetric. In order to describe the thin liquid film, and by analogy with the notation of Bretherton [13], the origin of the vertical axis y is on the tube's wall and its direction is radially inward. The horizontal coordinate x is directed downstream, and the reference $x = 0$ will be changed, as convenient, during this work. In these coordinates, the axial and radial velocities are defined as u and v, respectively, with v being positive when directed towards the axis of the channel. The no-slip condition applies at the channel wall. The thickness of the liquid film surrounding the bubble is $h(x)$.

From the front cap of the bubble, the liquid film thickness $h(x)$ decreases monotonically along the front dynamic meniscus towards the back of the

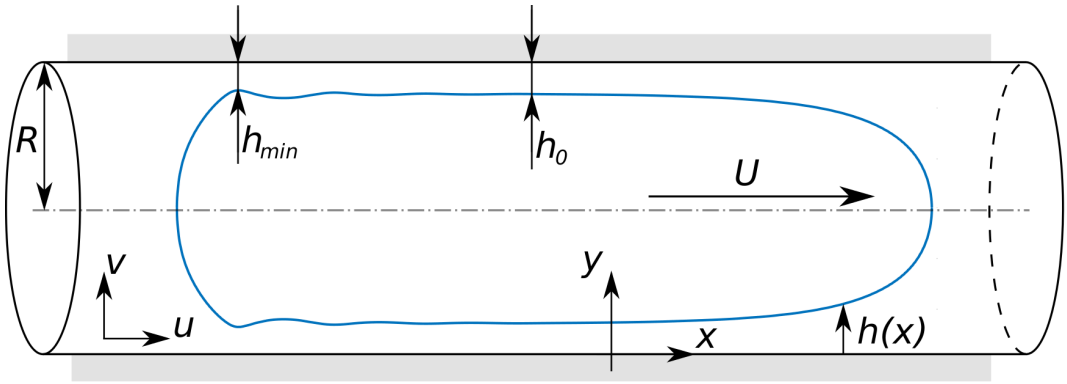

Figure 1: Sketch of a confined elongated bubble flowing within a tube and notation used in this work.

bubble, till a region of uniform film thickness h_0 is reached. The existence of such region for elongated bubbles will be confirmed by the numerical simulations. Along the rear dynamic meniscus, in the direction of negative x, the liquid film thickness $h(x)$ oscillates around h_0 and reaches a minimum value upon the most upstream crest of the interfacial wave. It eventually grows monotonically as the rear meniscus develops towards the rear cap of the bubble.

We assume that the flow is laminar, steady and incompressible, and that the fluid is Newtonian. The main flow structures characterizing the motion of the elongated bubble, i.e. liquid film thickness, front and rear menisci curvatures and wavelength of the interfacial wave, are fully determined by the capillary and Reynolds numbers [16, 17, 23]. For a circular channel, the characteristic length of the cross-section is $L = 2R$, and hence in this work the Reynolds number is defined as $\mathrm{Re} = 2\rho UR/\mu$. When the capillary number increases, viscous forces tend to make the liquid film thicker [13, 15]. An increase of the Reynolds number makes the liquid film thinner at intermediate values of Re ($\mathrm{Re} < 200$), while the opposite effect is observed at larger Re [27, 19]. Higher amplitude undulations on the bubble surface are associated with inertial effects that become relevant when $\mathrm{Re} \gg 1$ [22, 28].

3. Numerical model

Numerical simulations of the flow configuration reported in Fig. 1 are performed by means of the finite-volume opensource CFD package ESI OpenFOAM, release 2.3.1. The VOF-based `interFoam` solver is chosen to capture the interface dynamics. Below, the equations governing the numerical

model and the simulation setup are illustrated.

3.1. Governing equations and discretization methods

`interFoam` solves the Navier-Stokes equations for an incompressible flow and a Newtonian mixture fluid. According to the VOF formulation, the gas and liquid phases are treated as a single mixture fluid with variable properties across the interface, and a volume fraction α is defined to identify each phase on a fixed computational grid. The volume fraction represents the ratio of the cell volume occupied by the primary phase and hence ranges from 0 to 1. The volume fraction field, and thus the interface between the fluids, is transported by the flow field as:

$$\alpha_t + \nabla \cdot (\alpha \boldsymbol{u}) + \nabla \cdot [\alpha(1-\alpha)\boldsymbol{U_r}] = 0 \tag{1}$$

where $\boldsymbol{u}$ is the fluid velocity vector and $\boldsymbol{U_r}$ is an artificial compression velocity that counteracts numerical diffusion [29]. The subscript t indicates derivation versus time. The continuity and momentum equations solved by `interFoam` are:

$$\nabla \cdot \boldsymbol{u} = 0 \tag{2}$$

$$(\rho \boldsymbol{u})_t + \nabla \cdot (\rho \boldsymbol{u}\boldsymbol{u}) = -\nabla p + \nabla \cdot \mu \left[\nabla \boldsymbol{u} + (\nabla \boldsymbol{u})^T\right] + \sigma \kappa \boldsymbol{n} |\nabla \alpha| \tag{3}$$

where p is the pressure and the last term on the right-hand side corresponds to the surface tension force expressed according to the Continuum Surface Force method [30]. In our self-modified version of `interFoam`, the interface unit normal vector $\boldsymbol{n}$ and curvature κ are evaluated from a smoothed volume fraction field $\tilde{\alpha}$ [31]:

$$\boldsymbol{n} = \frac{\nabla \tilde{\alpha}}{|\nabla \tilde{\alpha}|}, \qquad \kappa = -\nabla \cdot \boldsymbol{n} = -\nabla \cdot \left(\frac{\nabla \tilde{\alpha}}{|\nabla \tilde{\alpha}|}\right) \tag{4}$$

The smoothed volume fraction field $\tilde{\alpha}$ is derived from the field α by interpolating the volume fraction values from the cell centre to the cell faces centres, and then back to the cell centre, two times.

First-order explicit and implicit schemes are utilized to discretize the volume fraction and momentum equations, respectively. Second-order TVD (Total Variation Diminishing) schemes are used for the spatial derivatives. The built-in MULES (Multidimensional Universal Limiter with Explicit Solution) algorithm [29] is adopted to discretize the last term of the volume fraction Eq. (1). The pressure-velocity coupling is solved by a PISO (Pressure Implicit Splitting of Operators) technique [32]. Simulations are run with a variable time-step calculated by the solver according to a maximum Courant number of 0.25. The convergence criterion for the iterative solution of the flow equations is based on the values of the absolute normalized residuals, 10^{-7} for the pressure and 10^{-6} for the velocity.

3.2. Simulation setup

The flow domain is modelled by adopting a 2D axisymmetric formulation. At the inlet boundary, liquid enters the flow domain with a fully developed parabolic velocity profile. At the channel wall, a no-slip condition is imposed. At the outlet boundary, the pressure is set to a zero reference value while the velocity gradient along the stream direction is set to zero [33]. An elongated bubble is initialized at the upstream end of the computational domain, see Fig. 2. The length of the bubble is $L_b \approx 20R$, such a length guarantees that a region of uniform film thickness exists between the front and rear menisci. The liquid flow rate at the domain inlet and the fluid properties for each simulation run are adjusted to match the target values of the capillary

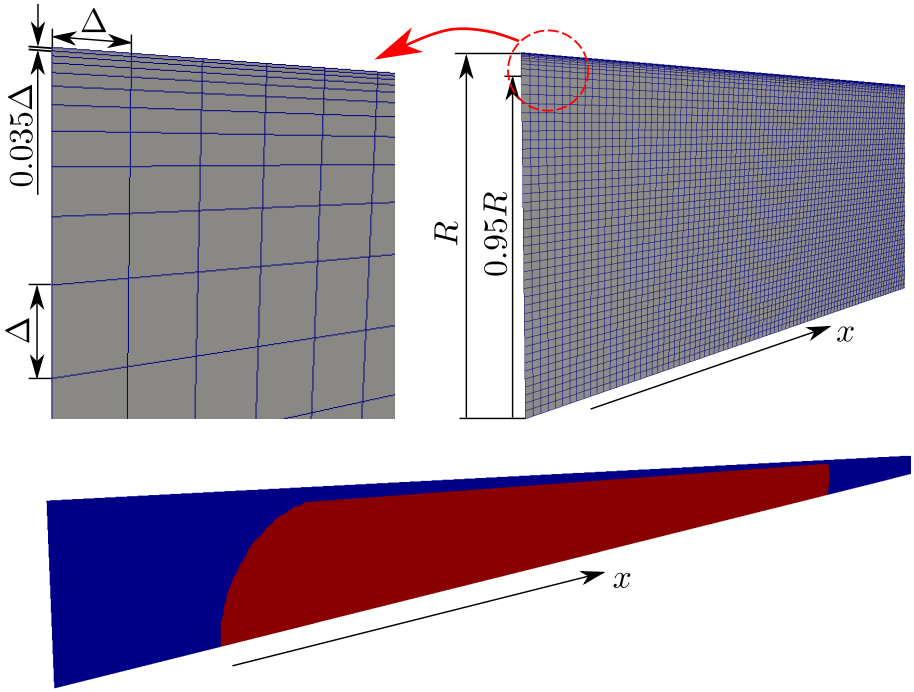

Figure 2: Illustration of the (top) computational mesh used for the CFD simulations with details of the near-wall refined grid and (b) shape and position of the bubble within the channel at $t = 0$. The size of the square mesh elements is $\Delta = 0.0238R$.

and Reynolds numbers. The liquid to gas density and viscosity ratios are respectively fixed to 1000 and 100. The CFD simulation is run in time until the bubble translates with a constant velocity.

The computational mesh is a structured orthogonal grid, see Fig. 2. From the axis of the channel to a distance of $0.05R$ from the wall, the mesh is made of uniform square cells of size $\Delta = 0.0238R$ (40 cells). At the near-wall region, the cells are gradually refined in order to capture the fluid mechanics within the thin liquid film surrounding the bubble. This region is discretized with 10 cells along the radial direction, with a maximum aspect ratio of 28.4.

This mesh arrangement was chosen upon a grid convergence test where both coarser ($20 + 6$ elements along y) and finer ($60 + 14$ and $80 + 18$) elements were tested.

The present numerical model was originally validated in Khodaparast et al. [23]. The authors obtained good agreement for the bubble shape, uniform liquid film thickness and bubble velocity with in-house experimental measurements under a large range of flow capillary numbers $10^{-4} < \mathrm{Ca} < 10^{-1}$ and Reynolds numbers $10^{-3} < \mathrm{Re} < 10^{3}$.

4. Lubrication model

A lubrication model is utilized to obtained predictions of the bubble profile, and thus of the uniform and minimum liquid film thicknesses. The model is based on the assumption that $h_0 \ll \ell$, with ℓ being a length scale for the front and rear menisci. The lubrication model is based on an extension of the classical axisymmetric Bretherton theory [13] and it accounts for inertia and for the curvature of the tube's wall. It was first developed by de Ryck [17] to describe the front meniscus of an air finger penetrating into a circular channel filled by liquid, and later adopted to investigate the undulations appearing at the rear meniscus of an elongated bubble in confined liquid flows by Magnini et al. [28]. The lubrication equations governing the flow within the liquid film in presence of inertial effects, to first order approximation,

read as follows:

$$u_x + v_y - \frac{v}{R-y} = 0 \tag{5}$$

$$\rho\left(uu_x + vu_y\right) = -p_x + \mu\left(u_{xx} + u_{yy} - \frac{u_y}{R-y}\right) \tag{6}$$

$$p_y = \mu\left[v_{yy} - \frac{v_y}{R-y} - \frac{v}{(R-y)^2}\right] \tag{7}$$

with boundary conditions:

$$u = v = 0 \qquad \text{at} \quad y = 0 \tag{8}$$

$$u_y = 0 \qquad \text{and} \quad p = -\sigma\kappa + 2\mu v_y \qquad \text{at} \quad y = h(x) \tag{9}$$

where the pressure inside the bubble is considered constant and is set to a zero reference value. The interface curvature is expressed as:

$$\kappa = \frac{h_{xx}}{(1+h_x^2)^{3/2}} + \frac{1}{(R-h)(1+h_x^2)^{1/2}} \tag{10}$$

Equations (5)−(9) are then replaced by equations integrated with respect to y. The direct method of Galerkin, as illustrated by Shkadov [34], Esmail and Hummel [35] and Koulago et al. [36], is then applied to express the velocity as a function of both x and y. By introducing the nondimensional variables $Y = h/h_0$ and $X = x/\ell$, with $\ell = h_0\mathrm{Ca}^{-1/3}$, this procedure leads to a third-order nonlinear differential equation for the nondimensional liquid film profile [17, 37]:

$$Y_{XXX} = 3\mathrm{Ca}^{2/3}\frac{Y_X Y_{XX}^2}{f_1} + \frac{HY_X}{\mathrm{Ca}^{2/3}(1-HY)^2}\left[\mathrm{Ca}^{2/3}(1-HY)Y_{XX} - Hf_1\right] +$$
$$+\left\{3\frac{(Y-1)}{Y^3}f_{2a} + \frac{1}{70}\,\mathrm{Re}\,\mathrm{Ca}^{1/3}H\frac{Y_X}{Y^3}f_{2b} + 3\frac{\mathrm{Ca}^{2/3}}{Y^3}\left[YY_{XX}f_{2c} + Y_X^2 f_{2d}\right]\right\} f_1^{3/2} \tag{11}$$

with:

$$f_1 = 1 + \mathrm{Ca}^{2/3} Y_X^2 \tag{12a}$$

$$f_{2a} = 1 + H\frac{Y-1}{2} \tag{12b}$$

$$f_{2b} = 6(Y^2 + Y - 9) + H\frac{134Y^3 - 171Y^2 - 1131Y + 1728}{32} \tag{12c}$$

$$f_{2c} = \frac{7Y - 33}{20} + H\frac{31Y^2 - 150Y + 99}{120} \tag{12d}$$

$$f_{2d} = \frac{2Y + 31}{10} + H\frac{2Y^2 + 19Y - 31}{20} \tag{12e}$$

where $H = h_0/R$ is the nondimensional liquid film thickness. Within Eq. (11), the first two terms at the right-hand side derive from the interface curvature, Eq. (10); the first term within curly brackets comes from the standard Bretherton problem, the second from the inclusion of inertia, and the third from the shear stress term within the boundary condition at the free surface. Details of the present derivation can be found in de Ryck [17] and Magnini et al. [28]. Equation (11) is integrated numerically towards the front ($X \to \infty$) or the rear ($X \to -\infty$) meniscus of the bubble. The integration starts from close to the flat film region using the linearized conditions $Y(X) = 1 + e^{sX}$, $Y_X(X) = se^{sX}$, $Y_{XX}(X) = s^2 e^{sX}$ where s is the solution of the third-order polynomial derived by linearization of Eq. (11) [17, 28].

This methodology yields theoretical profiles of the front and rear dynamic menisci of the bubble, from which the uniform h_0 and minimum film thickness h_{min} can be extracted.

5. Validation against experimental measurements

Magnini et al. [28] compared the uniform film thickness values obtained

with the present CFD and lubrication models with the predictions calculated by means of two widely used empirical correlations, for a range of capillary numbers of $0.002 \leq \mathrm{Ca} \leq 0.1$ and Reynolds numbers of $10^{-1} \leq \mathrm{Re} \leq 10^{3}$. Deviations were all within the accuracy band of the correlations, $\pm 15\%$.

Here, the CFD and the lubrication models are further benchmarked against the results of in-house experimental measurements of the liquid film thickness around elongated air bubbles transported by liquid in a circular microchannel. The test section is a straight horizontal FEP (Fluorinated Ethylene Propylene) circular tube. This is submerged in a liquid bath held within a transparent plexiglass container. The refractive indices of the tube wall material, the liquid in the medium surrounding the tube and the working liquid are approximately identical, this ensures that no optical distortion is present in the final images since the tube is observed through the flat surface of the fully transparent liquid bath. The liquid phase is pumped to the test section using a Mitos P-pump, while the bubbles are injected to the flow at a T-junction situated 15 cm upstream of the measurement point. A micro-particle shadow velocimetry technique (μPSV) is employed in the experimental measurements. This allows simultaneous quantification of important flow parameters (bubble speed, volume, liquid film thickness) using a sequence of high-speed greyscale images recorded at each test condition. A Nikon 10$\times$ Plan Fluor microscope objective, facing the test section from the top, is utilized to visualize the flow and a Photron FASTCAM SA3 high speed camera records the magnified images with a frame rate up to 10 kHz. The image resolution with the 10$\times$ magnification is of 1.824 μm/px. From the bubble images, see for instance Fig. 3(a), the uniform and minimum

thicknesses of the liquid film are extracted by image processing, and the velocity of the bubble is calculated by means of a time-strip technique [25]. Details about the experimental technique and post-processing methods are provided in Khodaparast et al. [38, 23]. The relative uncertainty on the film thickness measurements depends on the absolute value of the thickness and, for the data presented below, it ranges from 6% (at high Ca) to 28% (at low Ca) and from 12% to 40% for the uniform and minimum film thickness, respectively.

Experiments are performed in a circular tube of diameter of $D = 507\,\mu$m, using air ($\rho = 1.2\,\mathrm{kg/m^3}$, $\mu = 0.018\,\mathrm{mPa \cdot s}$) for the gas phase and methanol ($\rho = 791\,\mathrm{kg/m^3}$, $\mu = 0.521\,\mathrm{mPa \cdot s}$) for the liquid one, with a surface tension of $\sigma = 21.8\,\mathrm{mN/m}$. The flow conditions analyzed have capillary numbers ranging from 0.0036 to 0.024 and Reynolds numbers from 100 to 640. Very long, $L_b > 20R$, isolated bubbles are generated and run in the test section. Such a bubble length is necessary in order for a uniform film thickness region to exist between the front and rear menisci of the bubble in the visco-inertial ($\mathrm{Re} \gg 1$) regime [28]. This permits a univocal value of h_0 to be determined (i.e. not dependent on the location along the bubble where the measurement is performed), and ensures that the minimum film thickness does not depend on the bubble length.

Figure 3(a) presents a qualitative comparison of the shape of the rear meniscus of the bubble obtained with the experiment with those extracted from the CFD simulation and those from the numerical integration of Eq. (11), for a selected case. It can be seen that the profiles of the bubble, in terms of uniform and minimum thicknesses of the liquid film, and curvature of

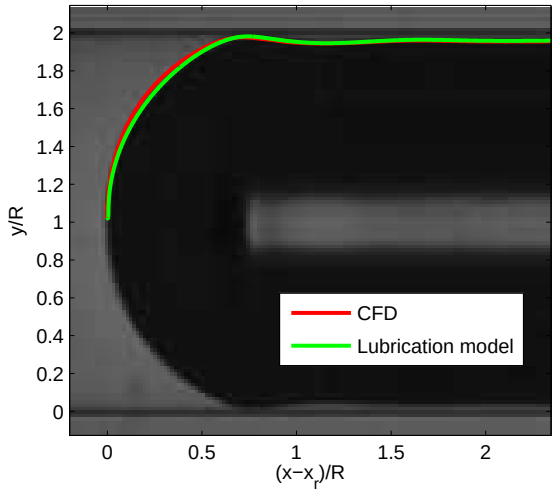

(a)

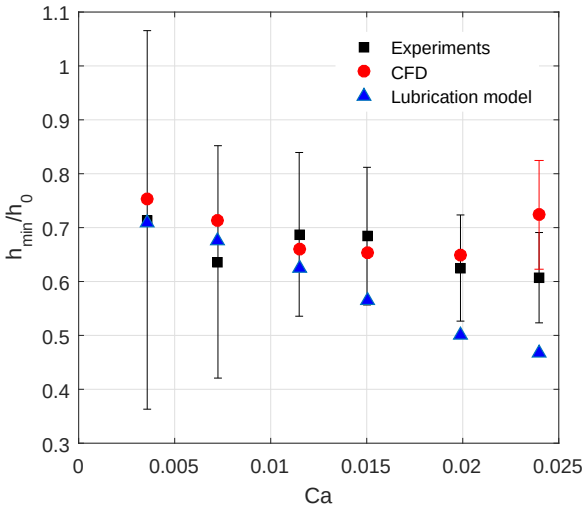

(b)

Figure 3: (a) Qualitative comparison of the bubble tail profile observed in the experiment and those obtained with a CFD simulation and the lubrication model for Ca = 0.0115 and Re = 300. x_r identifies the location of the tip of the bubble tail. Flow is from left to right. (b) Comparison of minimum film thickness values obtained with experiments (and their error band), CFD, and lubrication model.

the bubble tail, agree relatively well. A comparison of the normalized minimum liquid film thickness h_{min}/h_0 measured in the experiments and those obtained with the CFD and the theoretical model is given in Fig. 3(b). The CFD simulations always yield a value of the minimum film thickness which is very close to the experimentally measured value. At the highest Ca tested, time-dependent patterns on the bubble surface similar to those observed by Khodaparast et al. [23] and Ferrari et al. [39] occur in the simulations. For this reason, the data point for Ca = 0.024 included in the figure has to be intended as a time-averaged value, for which a temporal standard deviation of 10 % was observed in the CFD case. The range of temporal variation for this point is indicated as a red vertical band in Fig. 3(b). It is worth to note that the average value with its standard deviation is still within the uncertainty band of the experimental data point, which was measured by processing a single image frame. The lubrication model predicts values of the minimum film thickness that agree well with the experiments until Ca $\approx$ 0.012, while for larger capillary numbers the model systematically underpredicts the ratio h_{min}/h_0, thus exhibiting interfacial oscillations with larger magnitude than those resulting from the CFD simulations and experiments.

6. Results

CFD simulations and numerical integration of Eq. (11) are performed for a range of capillary numbers of $0.001 \leq \mathrm{Ca} \leq 0.5$ and Reynolds numbers of $0.1 \leq \mathrm{Re} \leq 2000$. Lower values of the capillary number fall within the range of validity of the Bretherton's model. For values of Ca = 0.5 and above, no undulations appear at the bubble tail, i.e. $h_{min}/h_0 = 1$. For each value

of the capillary number, the Reynolds number is varied from 0.1, where inertial effects are negligible and asymptotic conditions are achieved, to a maximum value at which time-dependent patterns begin to appear on the bubble surface. In the next sections, the effects of the capillary and Reynolds numbers on the undulations appearing in the proximity of the bubble tail are first discussed. A comparison of the rear meniscus shapes obtained with the CFD simulations and the lubrication model is presented. The outcome of a systematic analysis of the minimum film thickness values is finally provided.

6.1. Effect of capillary and Reynolds numbers

A qualitative analysis of the impact of the capillary and Reynolds numbers on the topology of the rear meniscus undulations is presented in this section. The profiles of the bubble obtained with the CFD simulations at Ca = 0.005 and Re = $0.1 - 1000$ are shown in Fig. 4(a). As introduced in Section 2, interface undulations appear on the liquid film in the proximity of the rear cap of the bubble, in the form of sinusoidal waves whose amplitudes grow when approaching the rear meniscus. A minimum film thickness value is thus achieved between the wall and the most upstream wave crest near the bubble rear. For values of Re up to 10, the Reynolds number does not have any appreciable effect and the profiles overlap. For Re $\geq$ 100, the liquid film thickness increases with Re as already observed by many authors [16, 17, 27]. More wave crests become visible on the surface of the bubble, as their amplitude, measured as $h_0 - h_{min}$, increases. This has been traditionally attributed to inertial effects [21, 40], and the theoretical work of Magnini et al. [28] demonstrated it rigorously. The inset in Fig. 4(a) plots the same data in the rescaled h/h_0 variable, and it can be seen that also the maximum

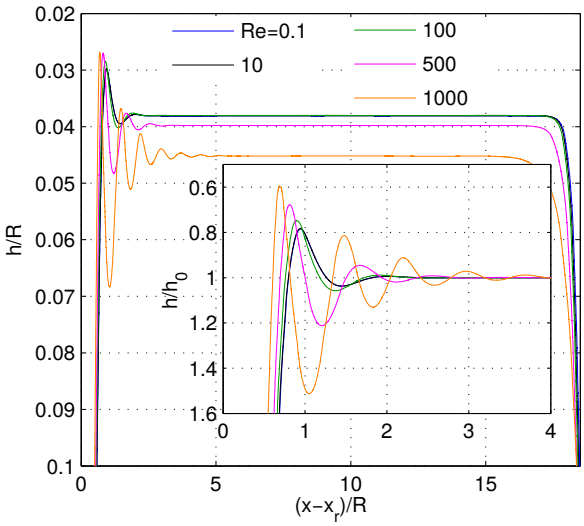

(a)

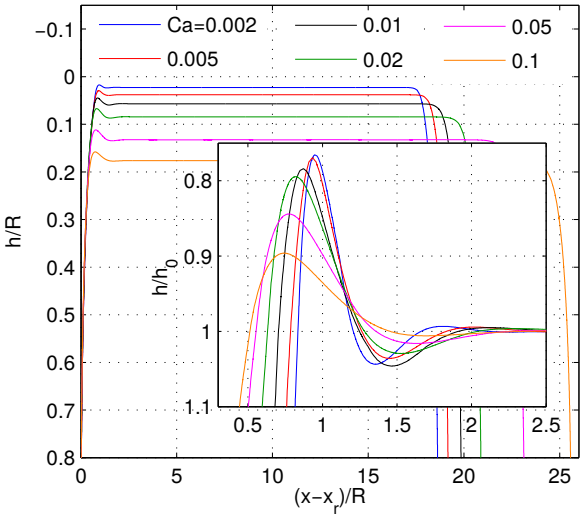

(b)

Figure 4: Profiles of the bubble obtained by CFD simulations for (a) Ca = 0.005 and different Reynolds numbers and (b) Re = 1 and different capillary numbers. x_r identifies the location of the tip of the bubble tail.

value of the relative wave amplitude $1 - h_{min}/h_0$ slightly grows with Re.

The profiles of the bubble at a constant Re = 1 (negligible inertial effects) and Ca = $0.002 - 0.1$ are depicted in Fig. 4(b). The uniform liquid film thickness increases with Ca as in the traditional Bretherton problem. Interestingly, the rescaled profiles illustrated in the inset indicate that the relative amplitude of the undulations decreases as the capillary number is increased, such that the interfacial wave becomes gradually less apparent.

6.2. Comparison of the rear meniscus profiles

A comparison of the profiles of the bubble back obtained with the CFD simulations and the theoretical model is provided in Fig. 5 for two selected flow conditions. A low Weber number case, $\mathrm{We} = \mathrm{Ca}\,\mathrm{Re} = 0.01$, is presented in Fig. 5(a). The Weber number is a parameter that measures the importance of inertia and it has been observed that inertial effects are negligible when $\mathrm{We} < 0.1$ [41]. Under such conditions, Fig. 5(a) shows that the undulation at the bubble tail exhibits only one main crest and one main valley. The profile given by the CFD simulation agrees very well with that obtained by means of the lubrication model. The minimum film thickness is slightly underestimated by the theoretical model, but notably the model also captures well the shape of the rear cap of the bubble.

A relatively high Weber number case, We = 3, is shown in Fig. 5(b). The effects of inertia are now apparent as $3-4$ wave crests become clearly visible. The lubrication model captures very well the features of the capillary wave, with wavelength, decay rate of the undulations and minimum film thickness being in excellent agreement with the CFD data.

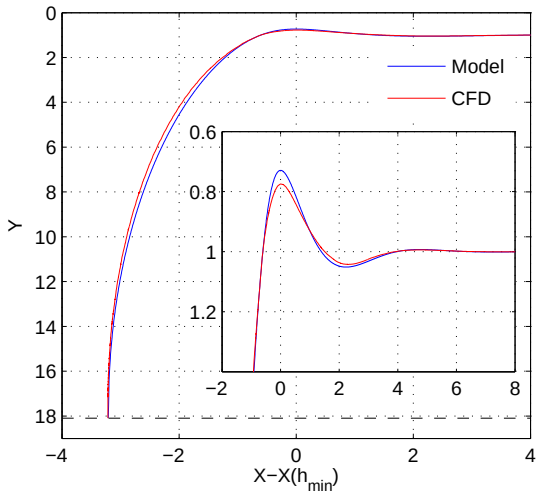

(a)

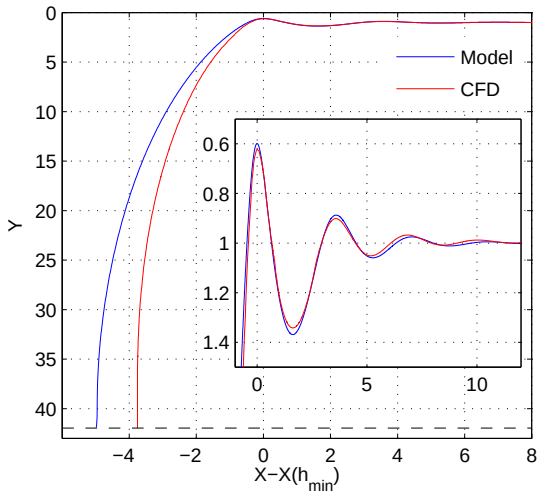

(b)

Figure 5: Comparison of the rear meniscus profiles obtained with the CFD simulations and by numerical integration of Eq. (11) for (a) Ca = 0.01 and Re = 1 and (b) Ca = 0.002 and Re = 1500. The horizontal black dashed lines identify the location of the axis of the tube. $X(h_{min})$ identifies the axial location where the minimum film thickness is measured at the rear meniscus.

6.3. Systematic analysis of the minimum film thickness

A systematic analysis of the effects of the capillary and Reynolds numbers on the minimum film thickness is now presented. The normalized minimum film thickness h_{min}/h_0 data extracted from the CFD simulations and from the lubrication model are plotted versus the Reynolds number in Fig. 6(a) and versus the Weber number in Fig. 6(b). It can be seen that the data points cluster very well when plotted versus We, where We = 0.1 is the threshold indicating the importance of inertial effects. When We $<$ 0.1, h_{min}/h_0 is independent of We for constant values of Ca. For We $>$ 0.1, the minimum film thickness decreases as the Weber number grows because the wave amplitude becomes larger.

The lubrication model yields values of h_{min}/h_0 that in the Re $\ll$ 1 range converge asymptotically towards about 0.72 as Ca is reduced, in agreement with the low capillary (Ca $\ll$ 1) and low Reynolds (Re $\ll$ 1) numbers theory of Bretherton [13], for which $h_{min}/h_0 = 0.716$. At Ca = 0.001, $h_{min}/h_0 \approx$ 0.74 in the CFD data and the theoretical value of $h_{min}/h_0 \approx 0.72$ seems to be an asymptotic limit, reached for values of the capillary number smaller than 0.001.

As the capillary number is increased, $h_{min}/h_0 \to 1$ and the undulations tend to flatten, in agreement with the trend of the rear meniscus profiles depicted in Fig. 4(b). At Ca = 0.5, $h_{min}/h_0 = 1$ for all the range of Weber numbers tested, $0.05 \leq$ We ≤ 50, so that waves are no longer observed and the bubble has a long cylindrical shape. The same asymptotic behavior was reported by Giavedoni and Saita [22] for the rear meniscus oscillations at large capillary numbers.

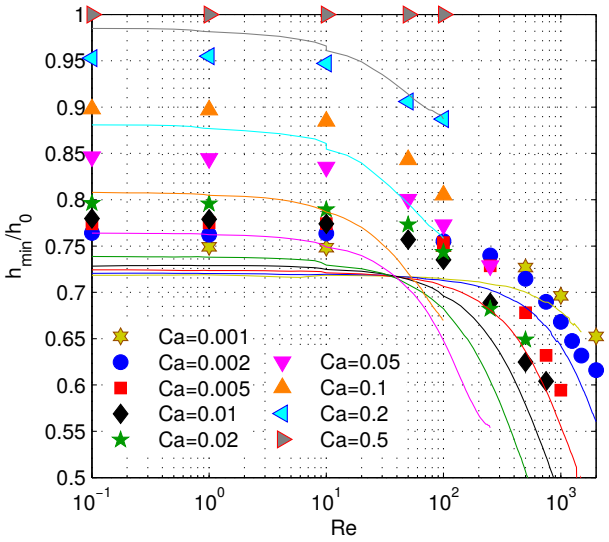

(a)

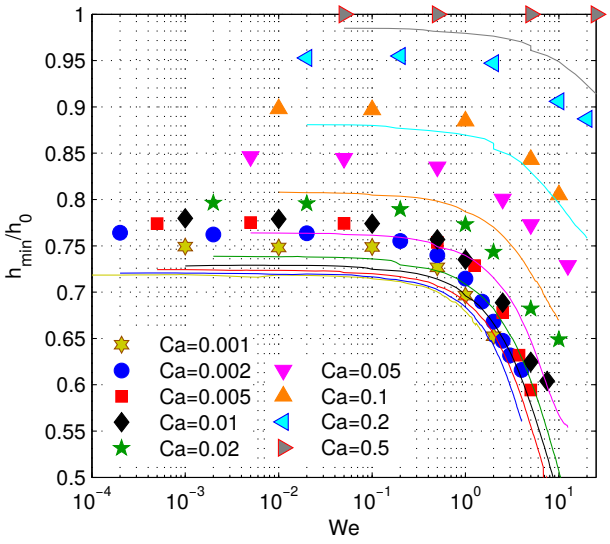

(b)

Figure 6: Minimum to uniform liquid film thickness ratio extracted from the CFD results (symbols) and from numerical integration of Eq. (11) (solid line) versus the (a) Reynolds number and (b) Weber number.

At low capillary numbers, Ca $\lesssim 0.01$, inertia leads to a remarkable reduction of the minimum film thickness, from about $0.75h_0$ when We < 0.1 to below $0.6h_0$ at We ≈ 10. Water, flowing within unsaturated pores of size of $0.1-1$ mm at Ca $= 10^{-4}-10^{-2}$, has We $= 10^{-4}-10$. Under such conditions, the crests of the waves along elongated bubbles may considerably approach the pore's wall, and therefore their interfacial surface tension may contribute to the detachment of wall-adhering micron-sized particles. This aspect is investigated more in detail in the next section.

The lubrication model systematically underpredicts the minimum film thickness, with increasing deviations as the capillary number grows. Note that the model is based on the assumption that Ca $\ll 1$, and therefore is not necessarily suitable to describe flow configurations with significant viscous effects. Nonetheless, the deviation with the CFD data is always within $15-20\%$.

7. Discussion

On the basis of the analysis above, the practical implications of thinning film processes on the fate of colloids deposited on the surface of a micro-pore is discussed.

When a gas-liquid interface comes in contact with a colloid adhering to a surface, a three-phase gas-liquid-solid contact line is formed on the surface of the colloid. Figure 7(a) presents a schematic of a spherical particle adhering to a micro-pore wall and interacting with the rear meniscus of an elongated bubble moving in a liquid flow. A continuous liquid film surrounds the bubble and wets the pore's wall. The necessary condition for the for-

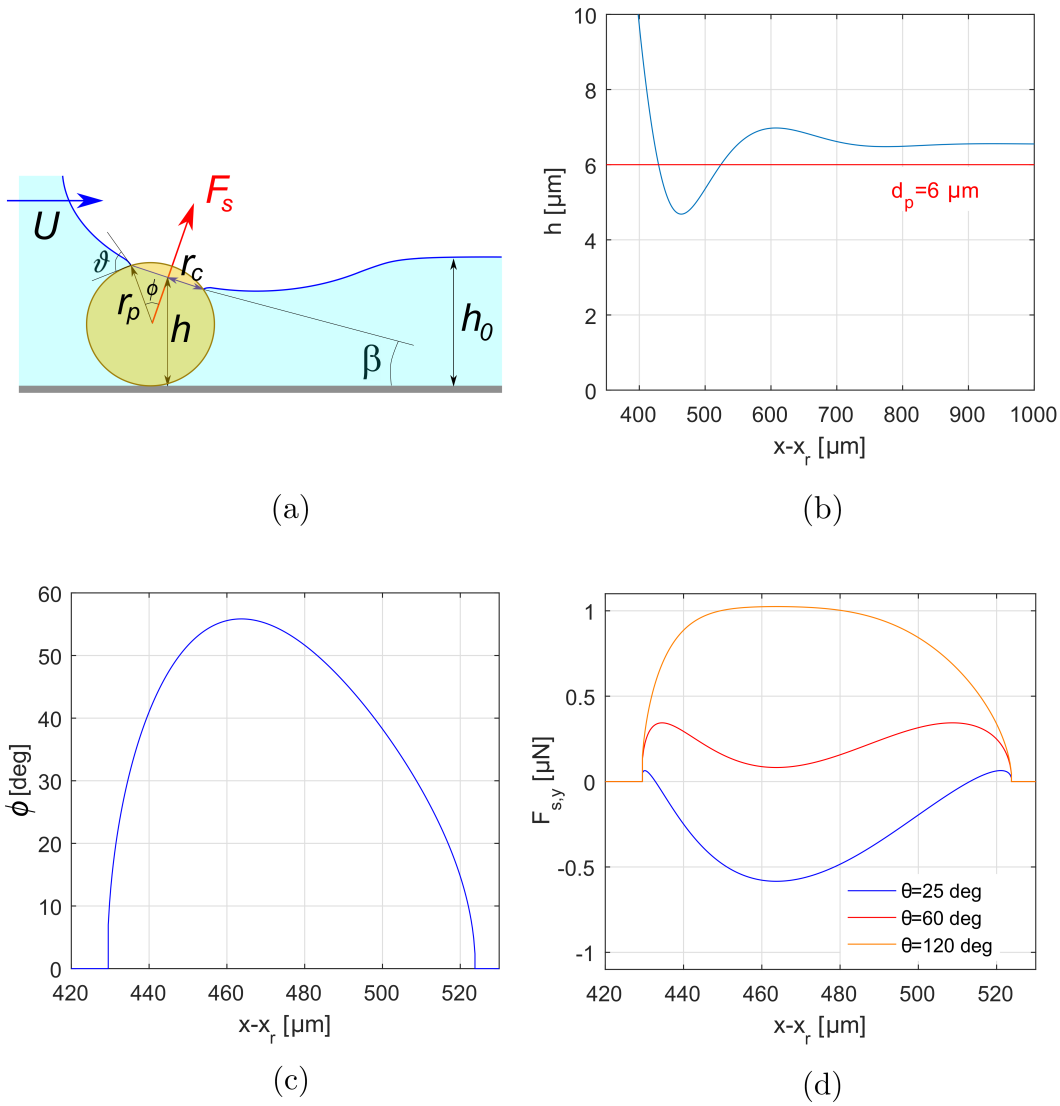

Figure 7: (a) Colloid interacting with the rear meniscus of an elongated bubble in confined flow. (b) Profile of the rear meniscus of a bubble for Ca = 0.001 and Re = 92 (in blue); the red line indicates the diameter of the colloid. Variation of (c) the filling angle and of (d) the vertical component of the capillary force exerted on the particle during the transit of the bubble. x_r identifies the location of the tip of the bubble tail.

mation of a contact line on the particle surface is $h(x) < d_p$, with d_p being the diameter of the colloid. The contact angle of the gas-liquid interface on the particle is denoted as θ and is considered constant. The filling angle, i.e. the angle between the normal to the plane where the contact line lays, and the line connecting the center of the sphere to any point on the contact line, is indicated as ϕ. β is the angle between the plane where the contact line lays and the pore's wall and it is assumed to be related to the local interface orientation, $\beta = \arctan(h_x)$.

The surface tension acting at the contact line exerts a capillary force of magnitude [6]:

$$|\boldsymbol{F_s}| = \sigma P \sin(\theta - \phi) \tag{13}$$

on the colloid, where P is the length of the contact line, $P = 2\pi r_c$, and r_c is the radius of the circular contact line on the particle surface, $r_c = r_p \sin\phi$, $r_p = d_p/2$. The filling angle is related to the local height of the interface relative to the channel wall, $h(x)$, as:

$$\phi = \arccos\left(\frac{h - r_p}{r_p \cos\beta}\right) \tag{14}$$

The vertical component of the capillary force $F_{s,y}$ depends on the local interface orientation:

$$F_{s,y} = \sigma P \sin(\theta - \phi)\cos\beta \tag{15}$$

and therefore it is a function of both $h(x)$ and $h_x(x)$. As such, if the gas-liquid interface is not flat, $F_{s,y}$ changes as the bubble is transiting upon the colloid. From Eq. (15), it follows that $F_{s,y} > 0$ when $\phi < \theta$, i.e. surface tension tends to remove the colloid from the pore's wall, while it opposes the

removal when $\phi > \theta$. Note that β is typically smaller than 5 degrees even for high amplitude interfacial undulations such as those depicted in Fig. 5(b), so that $\cos\beta \approx 1$ and:

$$F_{s,y} = \sigma 2\pi \sqrt{2hr_p - h^2} \sin\left[\theta - \arccos\left(\frac{h - r_p}{r_p}\right)\right] \tag{16}$$

We now consider a practical case in which a long air bubble travels in a circular pore of radius $R = 0.5\,\text{mm}$ in a water flow at $\text{Ca} = 0.001$ and $\text{Re} = 92$ ($U = 0.082\,\text{m/s}$). The lubrication model presented in this work predicts a uniform liquid film of thickness $h_0 = 6.5\,\mu\text{m}$, with a profile of the rear meniscus exhibiting one main undulation crest, as illustrated in Fig. 7(b).

We consider a spherical colloid adhering to the pore's wall with properties similar to those of the hydrophilic polystyrene particles of Gao et al. [7], $d_p = 6\,\mu\text{m}$ and $\theta = 25\,\text{deg}$. If the liquid film is assumed flat, as traditionally done in previous works [3, 4, 14], no interaction occurs among the colloid and the gas-liquid interface because $h_0 > d_p$. However, the present lubrication model yields a minimum film thickness of $h_{min} = 4.7\,\mu\text{m}$, thus suggesting that the bubble and the particle actually interact due to the undulation at the rear meniscus, where $h(x) < d_p$ (see Fig. 7(b)). This generates a profile of the filling angle ϕ that changes as the gas-liquid interface is moving upon the colloid as plotted in Fig. 7(c) ($h(x)$ and $h_x(x)$ are assumed not to be influenced by the contact with the particle).

The corresponding force exerted by surface tension on the colloid can be calculated by means of Eq. (16) and is plotted in Fig. 7(d). This force promotes detachment of the particle only at the initial and terminal stages of contact line formation and disappearance, when $\phi < \theta$ and $F_{s,y} > 0$,

while it pushes the particle against the wall during most of the contact period. This configuration changes substantially when partially hydrophobic ($30^\circ < \theta < 90^\circ$) and hydrophobic ($\theta > 90^\circ$) colloids (classification according to Petkov and Denkov [42]) are considered. Figure 7(d) shows that, under the same bubble flow condition, hydrophobic colloids may be subjected to detaching capillary forces of magnitude on the order of $F_{s,y} \approx 10^{-6} - 10^{-7}$ N. Given that the colloid adhesion force to the pore's wall, traditionally estimated by means of the Derjaguin-Landau-Verwey-Overbeek (DLVO) theory, is on the order of 10^{-8} N and below [10, 4, 14], the undulation of the bubble rear meniscus actively contributes to the detachment of the particle. This emphasizes the importance of accounting for the actual profile of the liquid film when analyzing colloid mobilization data. For instance, Khodaparast et al. [12] observed that bacteria adhering to a microchannel wall were removed by the transit of the rear meniscus of an elongated bubble at Ca > 0.001, despite the presence of a continuous liquid film around the bubble. The authors suggested that this could be related to a localized thinning of the liquid film at the channel wall nearby the bubble tail, although no quantitative measurements of the local film thickness were available to substantiate this hypothesis. Therefore, the present work opens a new horizon on the analysis of colloid mobilization by moving gas-liquid interfaces on solid substrates such as in unsaturated porous media, which may contribute to a better interpretation of experimental observations and natural phenomena.

8. Conclusions

In this article, we presented a systematic analysis of the shape of the rear meniscus of long bubbles in confined gas-liquid flows for both the visco-capillary ($\mathrm{Re} \ll 1$) and visco-inertial ($\mathrm{Re} \gg 1$) regimes. Pore-scale CFD simulations are utilized to generate bubble profiles in the capillary number range of $0.001 - 0.5$ and Reynolds number range of $0.1 - 2000$. A lubrication model based on the extension of the classical axisymmetric Bretherton theory is adopted to help understand the CFD results. Both the numerical and theoretical models are validated versus in-house experimental measurements of the minimum and uniform liquid film thicknesses around long air bubbles displaced by a liquid (methanol) flow. The lubrication model yields profiles of the rear meniscus of the bubble that agree reasonably well with the CFD results for the range of Ca and Re numbers of interest. The results of the present analysis indicate that inertial effects on the shape of the bubble become relevant when the Weber number of the flow, $\mathrm{We} = \mathrm{Ca}\,\mathrm{Re}$, grows above 0.1. In this regime, the amplitude of the interfacial wave appearing in the proximity of the bubble tail increases with the Reynolds number, such that the liquid film upon the crests of the undulations thins considerably, compared to its value in the central flat region of the bubble. Conversely, an increase of the capillary number tends to dampen the liquid film undulations, which are completely suppressed for $\mathrm{Ca} = 0.5$. In the low capillary number range, $\mathrm{Ca} \sim 10^{-3}$, which is characteristic of the flow of water in unsaturated porous media (e.g. soil), this study shows that the minimum liquid film thickness around long bubbles ranges from an asymptotic value of about $0.74h_0$ when $\mathrm{Re} \ll 1$, to below $0.6h_0$ when $\mathrm{Re} \sim 10^3$. Therefore, such

a localized thinning of the film may contribute to the detachment and mobilization of micron-sized colloids adhering to the pore's wall, e.g. particles, pollutants, or virus/bacteria, with important implications for the quality of drinking water resources.

Acknowledgements

M. Magnini is supported by the Swiss National Science Foundation (SNSF) under Contract No. 200020−156181. M. Magnini is grateful to S. Khodaparast (Department of Mechanical and Aerospace Engineering, Princeton University) for precious feedback during the development of this work.

References

[1] L. W. Lake, Enhanced Oil Recovery, Prentice Hall, 1989.

[2] S. Taku Ide, K. Jessen, M. O. J. Franklin, Storage of CO2 in saline aquifers: Effects of gravity, viscous, and capillary forces on amount and timing of trapping, Int. J. of Greenhouse Gas Control 1 (2007) 481–491.

[3] C. Gomez-Suarez, J. Noordmans, H. C. van der Mei, H. J. Busscher, Removal of colloidal particles from quartz collector surfaces as stimulated by the passage of liquid-air interfaces, Langmuir 15 (1999) 5123–5127.

[4] S. Aramrak, M. Flury, J. B. Harsh, Detachment of deposited colloids by advancing and receding air-water interfaces, Langmuir 27 (2011) 9985–9993.

[5] J. Wan, J. L. Wilson, Visualization of the role of the gas-water interface on the fate and transport of colloids in porous media, Water Resources Research 30 (1994) 11–23.

[6] A. F. M. Leenaars, A new approach to the removal of sub-micron particles from solid (silicon) substrates, in: K. L. Mittal (Ed.), Particles on Surfaces, Plenum Press, 1988, pp. 361–372.

[7] B. Gao, T. S. Steenhuis, Y. Zevi, V. L. Morales, J. L. Nieber, B. K. Richards, J. F. McCarthy, J.-Y. Parlange, Capillary retention of colloids in unsaturated porous media, Water Resources Research 44 (2008) W04504.

[8] J. E. Saiers, G. M. Hornberger, D. B. Gower, J. S. Herman, The role of moving air-water interfaces in colloid mobilization within the vadose zone, Geophysical Research Letters 30 (2003) 2083.

[9] Q. Zhang, S. M. Hassanizadeh, A. Raoof, M. T. van Genuchten, S. M. Roels, Modeling virus transport and remobilization during transient partially saturated flow, Vadone Zone Journal 11 (2012).

[10] Q. Zhang, S. M. Hassanizadeh, B. Liu, J. F. Schijven, N. K. Karadimitriou, Effect of hydrophobicity on colloid transport during two-phase flow in a micromodel, Water Resources Research 50 (2014) 7677–7691.

[11] V. Lazouskaya, Y. Jin, Colloid retention at air-water interface in a capillary channel, Colloid and Surfaces A: Physicochem. Eng. Aspects 325 (2008) 141–151.

[12] S. Khodaparast, M. K. Kim, J. Silpe, H. A. Stone, Bubble-driven detachment of bacteria from confined micro-geometries, Environmental Science & Technology 51 (2017) 1340–1347.

[13] F. P. Bretherton, The motion of long bubbles in tubes, J. of Fluid Mechanics 10 (1961) 166–188.

[14] V. Lazouskaya, L.-P. Wang, D. Or, G. Wang, J. L. Caplan, Y. Jin, Colloid mobilization by fluid displacement fronts in channels, J. of Colloids and Interface Science 406 (2013) 44–50.

[15] G. I. Taylor, Deposition of a viscous fluid on the wall of a tube, J. of Fluid Mechanics 10 (1960) 161–165.

[16] P. Aussillous, D. Quéré, Quick deposition of a fluid on the wall of a tube, Physics of Fluids 12 (2000) 2367–2371.

[17] A. de Ryck, The effect of weak inertia on the emptying of a tube, Physics of Fluids 14 (2002) 2102–2108.

[18] M. Heil, Finite Reynolds number effects in the Bretherton problem, Physics of Fluids 13 (2001) 2517–2521.

[19] Y. Han, N. Shikazono, Measurement of the liquid film thickness in microtube slug flow, Int. J. of Heat and Fluid Flow 30 (2009) 842–853.

[20] D. R. Langewisch, J. Buongiorno, Prediction of film thickness, bubble velocity, and pressure drop for capillary slug flow using a CFD-generated database, Int. J. of Heat and Fluid Flow 54 (2015) 250–257.

[21] R. Edvinsson, S. Irandoust, Finite-element analysis of Taylor flow, AIChE Journal 42 (1996) 1815–1823.

[22] M. Giavedoni, F. Saita, The rear meniscus of a long bubble steadily displacing a Newtonian liquid in a capillary tube, Physics of Fluids 11 (1999) 786–794.

[23] S. Khodaparast, M. Magnini, N. Borhani, J. R. Thome, Dynamics of isolated confined air bubbles in liquid flows through circular microchannels: an experimental and numerical study, Microfluid Nanofluid 19 (2015) 209–234.

[24] M. Magnini, J. R. Thome, A CFD study of the parameters influencing heat transfer in microchannel slug flow boiling, Int. J. of Thermal Sciences 110 (2016) 119–136.

[25] N. Borhani, B. Agostini, J. R. Thome, A novel time strip flow visualization technique for investigation of intermittent dewetting and dryout in elongated bubble flow in a microchannel evaporator, Int. J. of Heat and Mass Transfer 53 (2010) 4809–4818.

[26] C. W. Hirt, B. D. Nichols, Volume of fluid (VOF) method for the dynamics of free boundaries, J. of Computational Physics 39 (1981) 201–225.

[27] M. T. Kreutzer, F. Kapteijn, J. A. Moulijn, C. R. Kleijn, J. J. Heiszwolf, Inertial and interfacial effects on pressure drop of Taylor flow in capillaries, AIChE Journal 51 (2005) 2428–2440.

[28] M. Magnini, A. Ferrari, J. R. Thome, H. A. Stone, Undulations on the surface of elongated bubbles in confined gas-liquid flows, Physical Review Fluids 2 (2017) 084001.

[29] OpenFOAM User Guide, http://www.openfoam.org, 2016.

[30] J. U. Brackbill, D. B. Kothe, C. Zemach, A continuum method for modeling surface tension, J. of Computational Physics 100 (1992) 335–354.

[31] B. Lafaurie, C. Nardone, R. Scardovelli, S. Zaleski, G. Zanetti, Modelling merging and fragmentation in multiphase flows with SURFER, J. of Computational Physics 113 (1994) 134–147.

[32] R. I. Issa, Solution of the implicitly discretized fluid flow equations by operator-splitting, J. of Computational Physics 62 (1985) 40–65.

[33] S. V. Patankar, Numerical Heat Transfer and Fluid Flow, Hemisphere Publishing, New York, 1980.

[34] V. Y. Shkadov, Wave flow regimes of a thin layer of viscous fluid subject to gravity, Izv. Akad. Nauk URSS Mekh. Zh. Gaza 2 (1967) 43–51.

[35] M. N. Esmail, R. L. Hummel, Nonlinear theory of free coating onto a vertical surface, AIChE Journal 21 (1975) 958–965.

[36] A. Koulago, V. Shkadov, D. Quéré, A. de Ryck, Film entrained by a fiber quickly drawn out of a liquid bath, Physics of Fluids 7 (1995) 1221–1224.

[37] A. de Ryck, Erratum: The effect of weak inertia on the emptying of a tube, Physics of Fluids 14 (2002) 4100.

[38] S. Khodaparast, N. Borhani, J. R. Thome, Application of micro particle shadows velocimetry (μPSV) to two-phase flows in microchannels, Int. J. of Multiphase Flow 62 (2014) 123–133.

[39] A. Ferrari, M. Magnini, J. R. Thome, A Flexible Coupled Level Set and Volume of Fluid (flexCLV) method to simulate microscale two-phase flow in non-uniform and unstructured meshes, Int. J. of Multiphase Flow 91 (2017) 276–295.

[40] M. D. Giavedoni, F. A. Saita, The axisymmetric and plane cases of a gas phase steadily displacing a Newtonian liquid - A simultaneous solution of the governing equations, Physics of Fluids 9 (1997) 2420–2428.

[41] A. de Ryck, D. Quéré, Inertial coating of a fibre, J. of Fluid Mechanics 311 (1996) 219–237.

[42] J. T. Petkov, N. D. Denkov, Dynamics of particles at interfaces and in thin films, in: A. T. Hubbart (Ed.), Encyclopedia of Surface and Colloid Science, Marcel Dekker, New York, 2002.